ACS Catalysis

pubs.acs.org/acscatalysis Research Article

Preferential Oxidation of CO in Hydrogen at Nonmetal Active Sites with High Activity and Selectivity

Yongjie Xi and Andreas Heyden*

Cite This: ACS Catal. 2020, 10, 5362−5370 Read Online

ACCESS | Metrics & More | Article Recommendations | Supporting Information

ABSTRACT: Preferential oxidation of CO in hydrogen (PROX) is an effective process for purification of H_2 gas streams containing CO. Conventional PROX catalysts are usually a platinum group or Au-based. However, low-cost PROX catalysts with high CO conversion and a wide operating temperature window are rare. Here, we design a PROX catalyst by harnessing the electronic atomic monolayer−metal support interaction between a single layer 2-D material and a metallic support. O_2 is physiosorbed on nitrogen-doped graphene, while it adsorbs highly activated on Ni(111)-supported nitrogen-doped graphene where the O−O bond can dissociate readily. The adsorbed atomic oxygen can subsequently react with CO or H_2. The proposed catalyst is expected to maintain its activity in the presence of water. Microkinetic modeling results suggest that the turnover frequency of O_2 consumption with a CO partial pressure of 0.01 bar is over 2/s at room temperature and the selectivity to CO_2 is ∼100%. As an oxidation catalyst, Ni(111)-supported nitrogen-doped graphene is predicted to be also highly active for ethylene epoxidation at 423 K. Thus, the present study suggests a direction for the design of various selective oxidation catalysts.

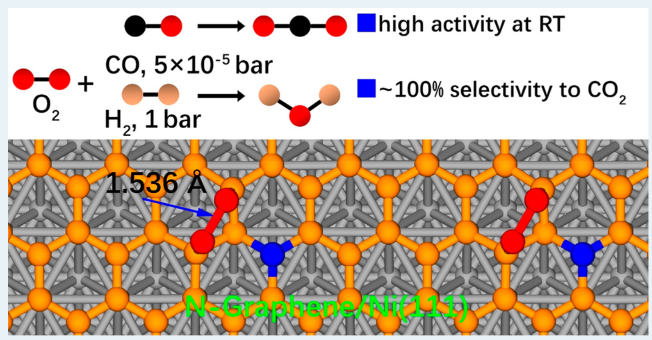

KEYWORDS: *CO oxidation, PROX, oxidation catalyst, ethylene epoxidation, graphene, DFT calculations*

1. INTRODUCTION

Hydrogen produced through methane steam reforming and water gas-shift (WGS) reactions contains ∼1% CO, which should be further purified to reduce the CO concentration below 50 ppm for applications in proton-exchange-membrane fuel cells (PEMFCs).[1−3] PROX is a promising cost-effective process for the removal of CO, as compared to CO methanation ($CO + 3H_2 \rightarrow CH_4 + H_2O$), which can consume up to 15% of the available H_2.[2] A benchmark goal of 50/50 was proposed for PROX catalysts, which means that the CO concentration in the product should be below 50 ppm and the O_2 selectivity to CO_2 should be above 50%.[1,2] Apart from the 50/50 goal, a good PROX catalyst should also have a wide operating temperature window (∼353−473 K) and high thermal stability.[4] Currently, platinum group metal (PGM) and Au-based catalysts are the most extensively explored PROX catalysts.[4] Pt catalysts typically possess high water stability, but the activity is low. To improve the activity of Pt catalysts, different preparation methods, oxide supports, and promoters were explored.[4] A Pt/Fe_2O_3 PROX catalyst featuring subnanometer Pt clusters[5] was found to be ∼100 times more active than a commercially available Pt/Al_2O_3 catalyst.[6] A recently reported inverse Pt-supported $Fe_1(OH)_x$ catalyst is about 10 times more active than a Pt/Fe_2O_3 PROX catalyst.[3] Other supported PGM catalysts including Ir,[7] Ru,[8] and Rh[9] were also explored as PROX catalysts. Au catalysts exhibit high PROX activity, but the selectivity to CO_2 decreases with an increase in temperature due to the oxidation of H_2. A single-atom Au/CeO_2 catalyst was found to suppress the oxidation of H_2, but it still suffers from a drop in CO_2 selectivity after 20 h of operation.[10] Apart from the activity loss of the catalyst, the presence of water can significantly affect the performance of Au catalysts. A recent study suggests that a commercial Au/Al_2O_3 catalyst exhibits optimal performance when two monolayers of water are adsorbed on the catalyst surface.[2]

Despite the remarkable progress in Au and PGM PROX catalysts, cost-effective PROX catalysts with high activity are still rare. For example, Cu-based catalysts have been extensively explored, but high conversion of CO is usually achieved only in a narrow temperature range.[11,12] To design a novel PROX catalyst, we consider the effect of a metal support, which manifests its importance in inverse catalysts.[13] It was, for example, revealed that a metal support enables electrocatalytic water oxidation on graphene monolayers by changing the

Received: February 12, 2020
Revised: April 11, 2020
Published: April 13, 2020

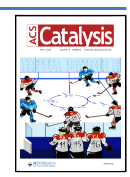

https://dx.doi.org/10.1021/acscatal.0c00743
ACS Catal. 2020, 10, 5362−5370

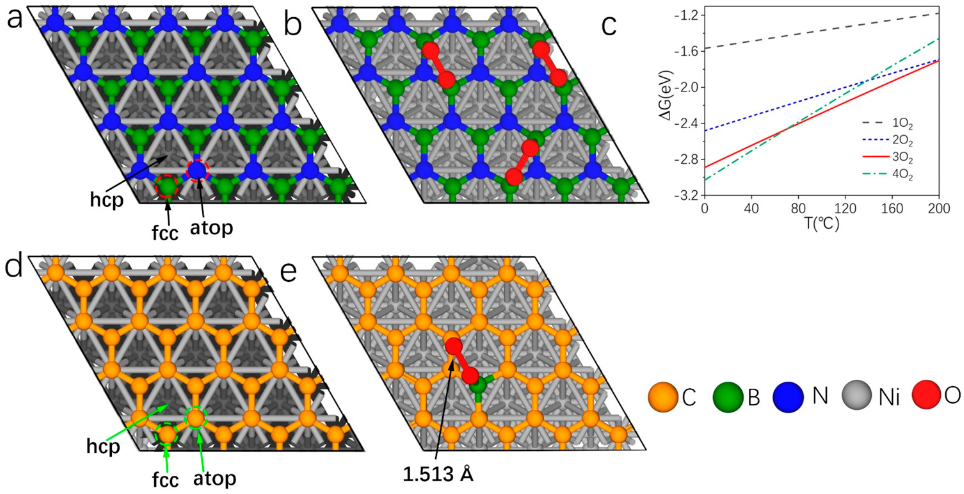

Figure 1. (a) Adsorption configuration of hBN on a five-layer (4 × 4) Ni(111) support; (b) adsorption of three O_2 molecules on hBN/Ni(111); (c) Gibbs free energies of O_2 adsorption on hBN/Ni(111) at various coverages, with the O_2 partial pressure set to 0.01 bar; (d) adsorption of graphene on a 4 × 4 Ni(111) support; and (e) adsorption of one O_2 molecule on B-GR/Ni(111).

electronic properties of graphene (GR).[14] Also, we have recently shown that Ni(111)-supported Rh-doped graphene exhibits comparatively high activity for direct methane to methanol oxidation and that overoxidation of methanol can be significantly reduced. In contrast, free-standing Rh-doped graphene has high reaction barriers for methane C−H activation, highlighting the importance of the effect of the Ni(111) support.[15] The tunability of the catalytic activity of doped graphene by a metal support offers enormous opportunities for the design of new catalysts. In the present study, we seek to design Ni(111)-supported monolayer catalysts for PROX reaction. While Ni(111)-supported pristine GR[16] is not able to chemisorb O_2 and hexagonal boron nitride (hBN)[17] is not able to catalyze CO oxidation with a reasonably high reaction rate (vide infra), we show in this Article that boron-[18] or nitrogen-doped[19] graphene (B-GR or N-GR) supported on Ni(111) can chemisorb O_2 with a moderate adsorption energy. We therefore examined CO and H_2 oxidation on B-GR/Ni(111) and N-GR/Ni(111). After determining various reaction pathways, we developed a microkinetic reaction model to understand the activity and selectivity of the catalyst. Finally, we demonstrate that N-GR/Ni(111) is potentially an oxidation catalyst for various reactions by examining the energy profiles of ethylene epoxidation.

2. COMPUTATION METHODS AND MODEL

First-principles calculations were performed using periodic density functional theory (DFT), as implemented in the Vienna Ab initio Simulation Package (VASP 5.4.4).[20,21] The spin-polarized generalized gradient approximation (GGA) with the PBE functional[22] was used to treat exchange-correlation effects. A plane wave basis set with a cutoff energy of 400 eV was selected to describe the valence electrons. The energy difference between reaction energies computed with a 400 and 500 eV cutoff was found to be smaller than 5 meV. The electron−ion interactions were described by the projector augmented wave (PAW)[23,24] method. Brillouin zone integration was performed with a 3 × 3 × 1 Monkhorst−Pack[25] (MP) k-mesh and Gaussian smearing (σ = 0.1 eV). We used Grimme's DFT-D3[26] scheme to treat the van der Waals interactions semiempirically. PBE-D3 calculations suggest that a graphene layer is 2.17 Å above the outermost plane of the Ni(111) support, which agrees well with the experimental value of 2.1 Å.[16] Other functionals such as RPBE[27] or revPBE[28] fail to describe the chemisorption of graphene on Ni(111). Because the graphene−Ni(111) interactions can also be well described by the SCAN functional with a long-range van der Waals interaction from rVV10,[29] we compared the energetics of selected reaction steps computed with SCAN +rVV10 and PBE-D3. While the chemisorption energy of O_2 is stronger when computed with SCAN+rVV10 by 0.34 eV, the physisorption energy of CO is not sensitive to the choice of functional, and, as discussed in more detail in the Supporting Information, the overall kinetics is only marginally affected by the choice of functional.

The SCF and force convergence criteria for structural optimization were set to 1 × 10^{-5} eV and 0.01 eV/Å, respectively. The climbing image nudged elastic band (CI-NEB)[30] and dimer methods[31,32] were used to optimize the transition state structures to achieve a force criteria of 0.03 eV/Å. All transition states have been confirmed with the existence of one imaginary frequency whose corresponding eigenvector points in the direction of the reactant and product state.

Neighboring slabs were separated by at least 13 Å of vacuum. The adsorption energy of a gas-phase molecule is defined as E_{ads} = E(surface+adsorbent) − E(surface) − E(adsorbent). Next, the Ni(111) surface is represented by a five-layer (4 × 4) slab. The lattice parameter of Ni(111) is close to that of graphene (Ni(111), 2.49 Å; graphene, 2.46 Å). To construct a Ni(111) supported graphene, the lattice parameter of Ni(111) is adopted for our calculations. Such a small tensile strain does essentially not change the electronic properties of graphene as shown in Figure S1. Also, the change in lattice parameter from 2.46 to 2.49 Å leads to only a small energy penalty of 0.16, 0.10, and 0.26 eV for a pristine (4 × 4) graphene, a boron-doped graphene, and a nitrogen-doped graphene, respectively, which is easily overcome by chemisorption on Ni(111). We also considered a six-layer Ni(111)-support model, and the calculated adsorption energy difference of O_2 on N-GR/Ni(111) using the six-layer and the five-layer model is less than 0.01 eV. Thus, we used the five-layer model for all subsequent calculations.

Next, the harmonic transition state theory was used to calculate all elementary rate constants of surface processes. Collision theory with a sticking coefficient of 1 was used to estimate the rate constants for adsorption processes. Using the obtained rate constants of each elementary step, we developed a chemical master equation of probability densities for the system to occupy each discrete state and solved for the steady-state solution. No assumption of active site coverage was made in the kinetic model. Details of our rate constant are provided in the Supporting Information. Finally, the energy of O_2 is adjusted to fit the experimental reaction energy of hydrogen combustion, $2H_2 + O_2 \rightarrow 2H_2O$, and increased by 0.49 eV to correct the overbinding[33] of O_2 predicted by the PBE functional.[15] A correction to the energy of O_2 lowers the free energy of each intermediate and transition state along the energy profile by 0.49 eV, while the energy barriers are not affected.

3. RESULTS AND DISCUSSION

3.1. Adsorption of O_2 on B-GR/Ni(111). Our attempt of identifying promising PROX catalysts starts from hBN/Ni(111) (Figure 1a) where boron is situated at the hcp site and nitrogen is situated at the atop site, respectively.[34] The chemisorption energy of hBN on a (4 × 4) Ni(111) was calculated to be −3.93 eV. O_2 molecules were found to be chemisorbed strongly on hBN/Ni(111) with the neighboring boron atoms occupied by two oxygen atoms (Figure 1b), which contrasts the case of free-standing hBN where O_2 is only physiosorbed. Bader charge analysis[35] suggests that a (4 × 4) hBN layer has a total negative charge of −1.13 $|e^-|$, indicative of the formation of chemical bonds between hBN and Ni(111). Upon the chemisorption of O_2, Ni(111) can serve as an electron reservoir and compensate the loss of electrons transferred from hBN to O_2. Each chemisorbed O_2 has a negative charge of ca. −1.8 $|e^-|$ and the O−O bond length is elongated to a range of 1.46−1.50 Å, depending on the number of O_2 molecules on hBN/Ni(111). Therefore, the presence of a Ni(111) support leads to a significant modification of the properties of hBN. Constrained thermodynamics calculations suggest that up to three O_2 molecules can be accommodated on a (4 × 4) hBN/Ni(111) at 80 °C and at a O_2 partial pressure of 0.01 bar (Figure 1c), following the typical operation conditions of the PROX reaction.[10] We therefore investigated the oxidation of CO on hBN/Ni(111) loaded with three O_2 molecules (Figure S2). However, we observed a free energy barrier of 1.19 eV (80 °C, CO partial pressure is 0.01 bar), corresponding to a forward rate constant of only 7.89×10^{-5}/s, suggesting that hBN/Ni(111) is not a good candidate for catalyzing CO oxidation under PROX reaction conditions. Next, we considered the case of Ni(111)-supported graphene. Our calculations suggest that GR is preferably adsorbed on Ni(111) with an atop/fcc configuration (Figure 1d), consistent with a previous study.[16] The adsorption energy is calculated to be −2.10 eV for a (4 × 4) graphene layer. However, O_2 can only be physiosorbed on GR/Ni(111). Considering that in the case of hBN/Ni(111) O_2 can be adsorbed strongly on a boron site, we speculated that the presence of a boron dopant in GR/Ni(111) can also lead to the chemisorption of O_2. We note that boron-doped graphene (B-GR) has previously been synthesized and used as an electrocatalyst.[18] A carbon atom on top of the Ni fcc site was replaced with a boron atom to construct our atomistic model shown in Figure 1d, which is the most favorable adsorption configuration (Figure S3), and the adsorption energy of B-GR on Ni(111) was calculated to be −4.03 eV. A Bader charge calculation suggests that B-GR gains 1.39 e^- from Ni(111).

The O−O bond is elongated to 1.513 Å upon adsorption on B-GR/Ni(111) (see Figure 1e). One oxygen binds to a fcc carbon, while the other one binds to boron. The chemisorption of O_2 on B-GR/Ni(111) contrasts that on free-standing B-GR where O_2 is only physiosorbed. Apart from O_2, all other investigated molecules in the present study (including CO) are physiosorbed on B-GR/Ni(111).

3.2. CO Oxidation on B-GR/Ni(111). Figure 2 illustrates the free energy diagram of CO oxidation on B-GR/Ni(111)

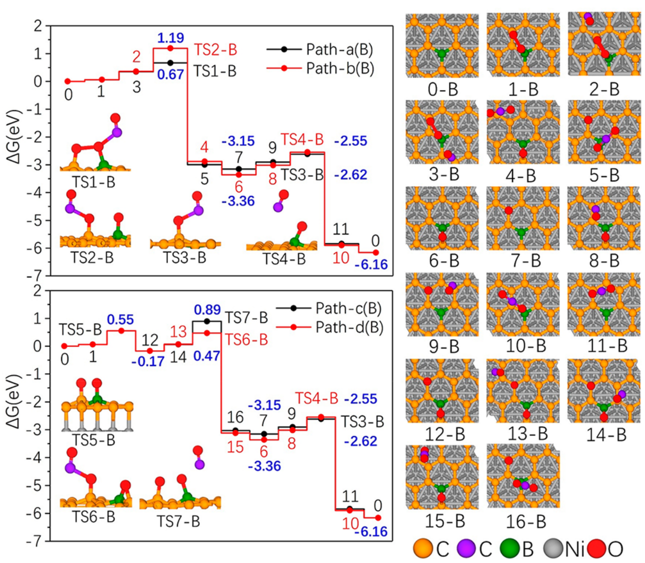

Figure 2. Free energy profiles of CO oxidation on B-GR/Ni(111) at 353 K. The partial pressures of all gas-phase molecules are set to be 1 bar. In **Paths-a(B)** and **-b(B)**, CO reacts with oxygen before O_2 dissociation occurs; in **Paths-c(B)** and **-d(B)**, CO reacts with atomic O. Boron doping is denoted as **B** in each intermediate and transition state. The **B** in each intermediate state along the energy profile is omitted for clarity. The description of each elementary is also presented in Table S1.

calculated at 353 K. CO can react with the pristine O_2 on B-GR/Ni(111) (see Figure 2, **Paths-a(B)** and **-b(B)**) or atomic O after the dissociation of the O−O bond (**Paths-c(B)** and **-d(B)**). The adsorption of O_2 is only slightly endergonic by 0.06 eV. In **Path-a(B)**, CO reacts with the O adsorbed at the boron site first, which is concomitant with the dissociation of the O−O bond and has an effective barrier of 0.67 eV (**3-B** → **5-B**; following the concept of the energy span model,[36] an effective barrier is calculated as the energy difference between a transition state and the lowest-energy intermediate preceding it). **5-B** → **7-B** and **4-B** → **6-B** correspond to the desorption of CO_2. The second CO reacts with the O adsorbed on the C site, and the effective barrier amounts to 0.53 eV (**9-B** → **11-B**). In **Path-b(B)**, CO reacts first with the O adsorbed at the carbon site. The effective barriers for CO oxidation along **Path-b(B)** are 1.19 and 0.81 eV, respectively.

The dissociation of the O−O bond has an effective barrier of 0.55 eV, whose free energy of reaction is exergonic by −0.17 eV (**1-B** → **12-B**). After O−O bond dissociation, one oxygen atom binds to one carbon atom in an upright configuration, while the other oxygen is shared by a boron and a carbon atom

https://dx.doi.org/10.1021/acscatal.0c00743
ACS Catal. 2020, 10, 5362−5370

(**12-B**, called B-bonded oxygen hereafter). The comparatively weak adsorption of oxygen on B-GR/Ni(111) is beneficial for the removal of oxygen by CO. The reaction of the C-bonded O with the first CO (**13-B** → **15-B**) has an effective barrier of 0.64 eV (**Path-d(B)**), while the reaction for the B-bonded O (**14-B** → **16-B**) has a barrier of 1.06 eV (**Path-c(B)**). The remaining parts of **Paths-c(B)** and **-d(B)** are identical to those of **Paths-a(B)** and **-b(B)**, respectively. Because an oxygen atom can migrate from a boron site to a carbon site (**6-B** → **7-B**) by overcoming a barrier of 0.84 eV (Table S4), the second CO oxidation can also occur through the pathway **6-B** → **7-B** → **9-B** → **11-B**. Throughout the process, an Eley−Rideal mechanism of CO oxidation is followed. Considering the energy profiles of **Paths-a**, **-b**, **-c**, and **-d(B)**, we can deduce that the first CO oxidation mainly proceeds through the path **12-B** → **13-B** → **15-B**. For the second CO oxidation, if the effective barrier of **6-B** → **TS4-B** → **10-B** (possible when the CO partial pressure is noticeably lower than 1 bar) is higher than that of the oxygen migration (**6-B** → **7-B**), then a **6-B** → **7-B** → **9-B** → **11-B** pathway is followed, which lowers the effective barrier by 0.07 eV relative to the pathway though **TS4-B**. In other words, the oxygen migration from the boron site to the carbon site can possibly lower the effective barrier of the second CO oxidation at lower partial pressures of CO due to the fact that **TS3-B** is 0.07 eV lower than **TS4-B**.

3.3. H_2 Oxidation on B-GR/Ni(111). For the reaction of H_2 with O_2 adsorbed on B-GR/Ni(111), we were unable to find an elementary reaction step involving the dissociation of O_2 and the formation of H_2O. In other words, O_2 dissociation has to occur prior to the reaction of atomic O with H_2. Because the H_2 molecule is only weakly physiosorbed on B-GR/Ni(111), an Eley−Rideal mechanism is again followed. Figure 3 illustrates that the reaction of the first H_2 with the O at the

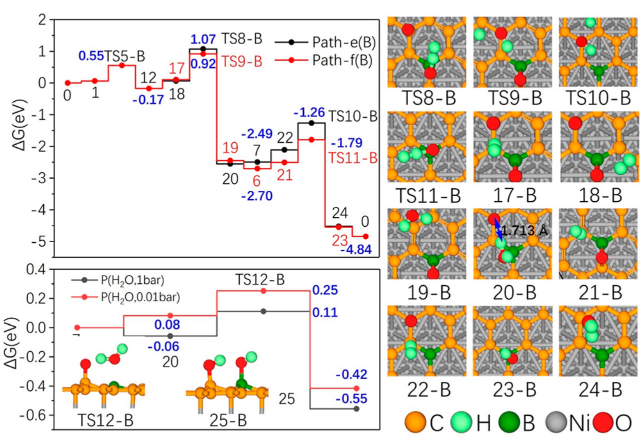

Figure 3. Free energy profiles of H_2 oxidation (above) as well as the formation of two hydroxyls by an oxygen atom and water (below) on B-GR/Ni(111) at 353 K. The partial pressures of all gas-phase molecules are set to be 1 bar. The description of each elementary is also presented in Table S1.

boron site has an effective barrier of 1.24 eV (**18-B** → **20-B**, **Path-e(B)**), as compared to the O on the carbon site, which has a barrier of 1.09 eV (**17-B** → **19-B**, **Path-f(B)**). Along **Path-e(B)**, the reaction of the second H_2 and the C-bonded O (**7-B** → **24-B**) has an effective barrier of 1.23 eV, while the reaction of the second atomic O (**6-B** → **23-B**) along **Path-f(B)** has a lower barrier of 0.91 eV. The reactions of H_2 with the boron-bonded oxygen feature early transition states (**TS8-B** and **TS11-B**, see TS configurations in Figures 3 and S4), while those involving the carbon-bonded oxygen feature late transition states (**TS9-B** and **TS10-B**). For the reaction of each oxygen atom, we observe that CO has a higher reactivity than does H_2, which is due to the fact that the formation of H_2O requires the insertion of the oxygen atom into the H−H bond of the physiosorbed H_2, while CO_2 is formed simply by the approach of CO to the adsorbed oxygen. Moreover, we examined the dissociation of H_2 on B-GR/Ni(111) in the absence of adsorbed oxygen, which has a high barrier of 2.40 eV and is endergonic by 1.12 eV (see Figure S5). From the above discussions, it is obvious that an oxygen atom bonded to a boron and a carbon has distinct reactivities. This can be traced back to the different adsorption configurations of oxygen in **6-B** and **7-B** where an oxygen atom binds to both boron and carbon atoms in the case of **6-B** and only to a carbon atom in the latter case of **7-B** (see Figure 2).

Under PROX reaction conditions, the presence of water is unavoidable. Therefore, we incorporated the presence of water in the reaction pathways on B-GR/Ni(111). **20-B** → **25-B** corresponds to the reaction of an adsorbed water and an oxygen atom, which produces two hydroxyl groups and has a low barrier of 0.17 eV at a water pressure of 1 bar (see Figure 3). At a water partial pressure of 0.01 bar, which is more typical for PROX reactors, the energy profile shown in Figure 3 suggests that **25-B** is 0.42 eV lower than **7-B**. The reaction of **25-B** and a physiosorbed CO may proceed through a COOH mechanism of CO oxidation,[37] which is common for chemisorbed CO and OH that can produce a COOH intermediate, followed by cleavage of the O−H bond to produce CO_2. However, we were not able to identify a COOH mechanism in the present case, likely because the approach of the CO to the B-GR/Ni(111) surface is energetically unfavorable. To react with CO, the two hydroxyl groups need to form an adsorb oxygen and a water molecule (**25-B** → **20-B**), followed by facile water desorption (**25-B** → **7-B**). Considering that the effective barrier of **6-B** → **TS4-B** → **10-B** at a CO partial pressure of 0.01 bar (PROX condition) is calculated to be 0.95 eV (i.e., it is higher than the oxygen migration barrier of 0.84 eV; see Table S4), the second CO oxidation preferably proceeds through **6-B** → **7-B** → **9-B** → **11-B** with an effective barrier of 0.88 eV. However, in the presence of H_2O (0.01 bar), the effective barrier of the second CO oxidation on B-GR/Ni(111) is increased by 0.42 eV, being 1.30 eV, which is translated to a low forward reaction rate of 2.03×10^{-6}/s. Thus, we can conclude that CO oxidation on B-GR/Ni(111) is poisoned by water dissociation under PROX reaction conditions.

3.4. CO and H_2 Oxidation on N-GR/Ni(111). Because B-GR/Ni(111) appears to be not a good active site model for a PROX catalyst, we next examined the PROX reaction on nitrogen-doped graphene supported on Ni(111). Again, various reaction pathways involving the dissociation of water were considered. We first identified the most favorable adsorption configuration of N-GR on Ni(111) shown in Figures 4a and S6, whose adsorption energy is −2.35 eV. Bader charge calculations suggest that the N-GR unit cell gains 1.58 e^- from Ni(111). We found that an O_2 molecule can be chemisorbed on N-GR/Ni(111) in three different configurations (Modes-a, -b, and -c in Figure 4b). In all cases, one or two next-nearest carbon atoms of the nitrogen site (C1−C6 in Figure 4a) are occupied by oxygen. We were unable to identify other chemisorption configurations of O_2 for which other

https://dx.doi.org/10.1021/acscatal.0c00743
ACS Catal. 2020, 10, 5362−5370

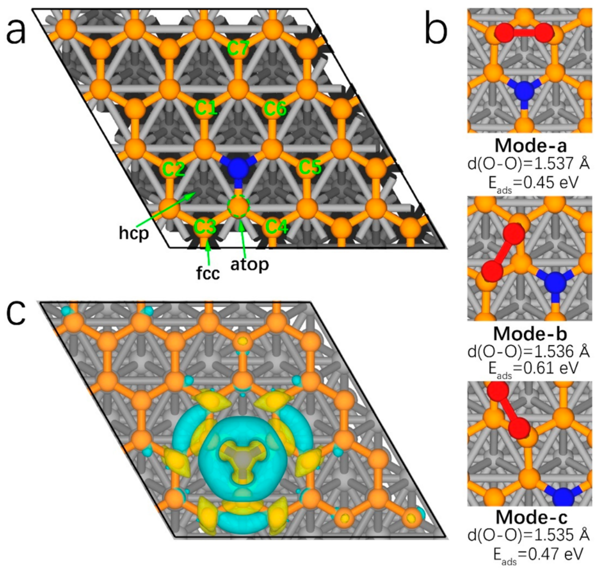

Figure 4. (a) Adsorption configuration of nitrogen-doped graphene on a five-layer (4 × 4) Ni(111) support. C1−C6 are equivalent carbon atoms. (b) Chemisorption configurations of O_2 on N-GR/Ni(111). (c) Charge density difference upon the deposition of nitrogen at Ni(111)-supported graphene with a carbon defect. The accumulation (depletion) of electrons is denoted by yellow (blue). The isosurface value is 0.003 $|e^-|/Å^3$.

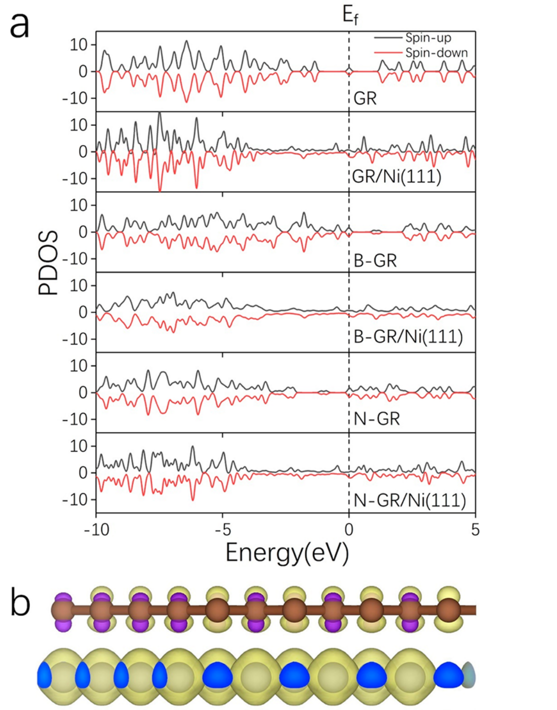

Figure 5. (a) Projected density of states of carbon for free-standing GR, B-GR, and N-GR as well as the Ni(111)-supported counterpart. The Fermi level is set to 0 eV. (b) Spin density of Ni(111)-supported pristine graphene. Spin-up (spin-down) electrons are denoted in yellow (purple). The isosurface value is 0.003 $|e^-|/Å^3$.

carbon atoms or the nitrogen site are adsorption sites of oxygen. A charge density difference plot suggests that, upon the deposition of nitrogen at the carbon defect site of GR/Ni(111), the charge surrounding the nitrogen atom redistributes and charge accumulation occurs on the six next-nearest carbon atoms (Figure 4c), C1−C6. In the case of free-standing N-GR, O_2 is only physiosorbed.

To further understand the activation of an O_2 molecule by the carbon atoms of N-GR/Ni(111), we plotted the projected density of states of carbon (PDOS, Figure 5a) for the free-standing and Ni(111)-supported GR, B-GR, and N-GR. The PDOS of carbon moves toward lower energies due to the interaction with Ni(111), which is indicative of electronic interaction between GR (or doped-GR) and Ni(111). Inspection of the PDOS near the Fermi level suggests that the electrons of carbon (supported on Ni(111)) have a small spin-polarization, which can be attributed to the broken sublattice symmetry of graphene[38,39] due to the presence of Ni(111). The spin-polarization of carbon is also reflected in the spin-density plot (Figure 5b), and each carbon atom has a magnetic moment of ∼0.03 μB. For the case of supported boron nitride, each boron has a magnetic moment of ∼0.02 μB. The spin-polarized carbon or boron facilitates the activation of O_2. However, an O_2 molecule is not chemisorbed (practically no change in O−O bond distance) on GR/Ni(111), likely due to the weaker adsorption of an oxygen atom on GR/Ni(111) (−0.71 eV) relative to the C1−C6 sites on N-GR/Ni(111) (Figure 4a, −0.87 eV) where the O−O bond distance is increased to 1.54 Å upon O_2 adsorption. Carbon atoms (e.g., C7 in Figure 4a) distant from the nitrogen-dopant have an oxygen adsorption of ∼ −0.73 eV (close to pristine graphene) and are not able to activate O_2. This is consistent with the fact that charge-redistribution due to the nitrogen-doping occurs at C1−C6.

We next examined the energy profiles (**Paths-a(N)** and **-b(N)**) of CO and H_2 oxidation for the most favorable O_2 adsorption configuration Mode-b, as displayed in Figure 6. O_2 adsorption is slightly endergonic at 353 K (**1-N**), followed by O−O dissociation, which involves a vanishingly small barrier. As compared to the O−O bond dissociation on B-GR/Ni(111), the more favorable O−O dissociation on N-GR/Ni(111) can be attributed to the fact that an upright

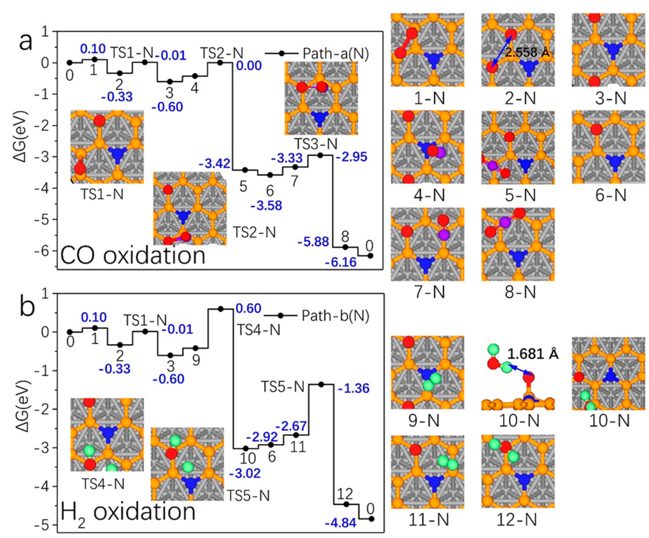

Figure 6. Free energy profiles of CO (a) and H_2 oxidation (b) on N-GR/Ni(111) at 353 K without the dissociation of H_2O. The partial pressures of all gas-phase molecules are set to be 1 bar. The description of each elementary is also presented in Table S2.

https://dx.doi.org/10.1021/acscatal.0c00743
ACS Catal. 2020, 10, 5362−5370

adsorption configuration of oxygen on boron in **TS5-B** is unfavorable for the B-GR/Ni(111). The two oxygen atoms of **2-N** have a comparatively short distance of 2.558 Å, and the migration of one oxygen to another carbon site leads to a decrease in free energy of 0.27 eV, which we attribute to a decrease in electrostatic repulsion between the negatively charged oxygen atoms. The physiosorbed CO can react with oxygen atoms adsorbed on N-GR/Ni(111) through the paths **3-N** → **4-N** → **5-N** and **6-N** → **7-N** → **8-N**, whose effective barrier we calculated to be 0.60 and 0.57 eV at 353 K, respectively. The H_2 oxidation possesses a significantly higher activation barrier than does the CO counterpart, being 1.20 eV for **3-N** → **9-N** → **10-N** and 1.56 eV for **6-N** → **11-N** → **12-N**, respectively. Note that the desorption of H_2O (**10-N** → **9-N**) is slightly endergonic at a high H_2O partial pressure of 1 bar due to the relatively strong hydrogen bond between hydrogen and oxygen (denoted as **10-N** in Figure 6b).

We also investigated reaction pathways (**Paths-c(N)** and **-d(N)**) of H_2 and CO oxidation on N-GR/Ni(111) involving the dissociation of water shown in Figure 7. Starting from **3-N**,

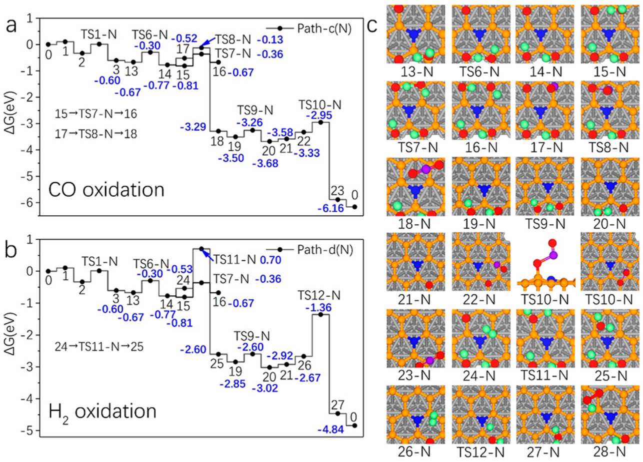

Figure 7. Free energy profiles of CO (a) and H_2 oxidation (b) on N-GR/Ni(111) at 353 K involving the dissociation of H_2O. (c) Configurations of all intermediate and transition states. The partial pressures of all gas-phase molecules are set to be 1 bar. The description of each elementary is also presented in Table S2.

oxygen can react with adsorbed H_2O to form hydroxyl groups. **14-N** featuring two hydroxyl groups is 0.17 eV lower in free energy than is **3-N**, whereas **16-N** featuring four hydroxyl groups is 0.10 eV higher in energy than is **14-N**. Therefore, the formation of hydroxyl groups on N-GR/Ni(111) is less thermodynamically favorable than the **7-B** → **20-B** → **25-B** counterpart of B-GR/Ni(111). **14-N** can react with CO by overcoming an effective barrier of 0.64 eV to form **18-N**. Upon the formation of the first CO_2, the two hydroxyl groups of **19-N** can form an adsorbed oxygen and H_2O, which is energetically downhill by 0.18 eV. While the **21-N** → **22-N** → **23-N** path occurs at an active site different from that of the **6-N** → **7-N** → **8-N** path (see Figures 6a and 7a), the energy profiles of the two processes are the same because the oxygen atoms of **21-N** and **6-N** are equivalent (see Figure 4). H_2 can also be oxidized on N-GR/Ni(111) in the same vein as CO through **14-N** → **24-N** → **25-N** and **21-N** → **26-N** → **27-N**, respectively, with noticeably higher activation energies than the CO oxidation. We emphasize here that the energetically uphill process of **14-N** → **15-N** → **16-N** and downhill process of **19N** → **20-N** → **21-N** (even if the H_2O partial pressure is 1 bar) ensure that no hydroxyl group poisoning occurs for the N-GR/Ni(111) catalyst. Apart from the reaction pathways in the absence/presence of H_2O, we also considered a reaction pathway involving an OOH species, which is a possible active species for CO oxidation.[40] Here, we found that the formation of an OOH species is energetically uphill by 1.25 eV (**14-N** → **28-N**), which is significantly higher than the effective barrier of CO oxidation (~0.6 eV) mentioned above. Therefore, an OOH pathway is unlikely to occur on N-GR/Ni(111).

To this end, we have examined the energy profiles of the CO and H_2 oxidation on B-GR/Ni(111) and N-GR/Ni(111). We found that, at 353 K, CO oxidation by an adsorbed oxygen at a carbon site has an effective barrier of around 0.60 eV, which is not sensitive to the environment of the active sites. In comparison, the effective barrier of H_2 oxidation at the carbon site ranges from 1.09 eV (**12-B** → **TS9-B** → **19-B**) to 1.56 eV (**6-N** → **TS5-N** → **12-N**), which can be correlated with the oxygen adsorption energy (see Figure 8). Hence, a lower

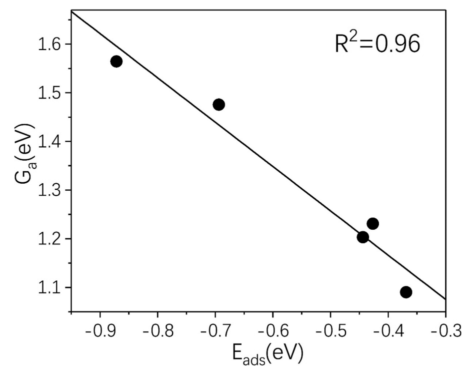

Figure 8. Scaling relation between the effective barrier (G_a, 353 K, the H_2 pressure is 1 bar) of H_2 oxidation by O adsorbed at the carbon site on B-GR/Ni(111) and N-GR/Ni(111) versus the O adsorption energy (E_{ads}). $G_a = 0.911 \times E_{ads} + 0.802$. The reference state of E_{ads} is the clean surface and $0.5O_2$ in the vapor phase.

oxygen adsorption energy is favorable for the formation of water. We note here that the scaling relation of H_2 oxidation on the C-bonded oxygen is not applicable for the B-bonded oxygen shown in Figure S7; that is, the scatter in the data is large, probably due to the different adsorption configuration of the B-bonded oxygen.

3.5. Microkinetic Modeling of CO and H_2 Oxidation on N-GR/Ni(111).

A microkinetic model was developed to understand the PROX reaction kinetics (see Tables S5−S8 for the rate constants of each elementary step). The microkinetic model was solved for a H_2 partial pressure of 1 bar. The CO partial pressure was set to be in the range of 5×10^{-5} and 0.01 bar.[10] A low CO pressure of 5×10^{-5} bar was considered due to the need to reduce the CO concentration to ~50 ppm.[1,2] The partial pressures of O_2, H_2O, and CO_2 were all set to be 0.01 bar. At 353 K and a CO partial pressure of 0.01 bar, the turnover frequency (TOF) of O_2 consumption was calculated to be 33.46/s, and the selectivity to CO_2 is ~100%. At a CO pressure of 5×10^{-5} bar, the selectivity to CO_2 still reaches ~100%. Figure 9 shows a low apparent activation energy of 0.45 eV for the oxygen consumption. The reaction orders of CO (from 5×10^{-5} to 0.01 bar) and O_2 (0.01−1 bar) were calculated to be 1 and 0 at 353 K, respectively. Even if the temperature deceases to 300 K, a high TOF of 2.38/s was

https://dx.doi.org/10.1021/acscatal.0c00743
ACS Catal. 2020, 10, 5362−5370

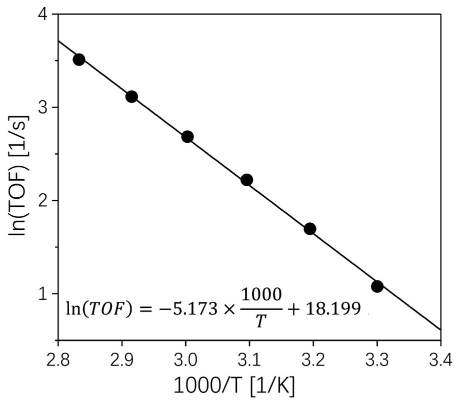

Figure 9. Arrhenius plot for CO/H_2 oxidation, that is, O_2 consumption, over N-GR/Ni(111) in the temperature range 300−353 K.

obtained, which is comparable to that found for Pt-supported $Fe_1(OH)_x$ (2.1/s).[3]

To better understand the high activity and selectivity of CO oxidation obtained from the microkinetic analysis, we plotted in Figures S8 and S9 the free energy profiles with a CO partial pressure of 0.01 bar. Along **Paths-a(N)** and **-b(N)**, the effective barriers of the first and second CO oxidation were calculated to be 0.74 and 0.77 eV, respectively, as compared to 1.20 and 1.56 eV for the oxidation of the first and the second H_2. If the dissociation of H_2O is involved in the reaction, the effective barrier for the first CO oxidation along **Path-c(N)** is 0.78 eV, as compared to 1.47 eV for the H_2 along **Path-d(N)**. The effective barriers of the second CO and H_2 oxidation along **Path-c(N)** and **Path-d(N)** are the same as those along **Path-a(N)** and **Path-b(N)**, respectively. Even if the CO partial pressure is reduced to 5×10^{-5} bar, the effective barriers of CO oxidation are only ~0.94 eV (see Figure S10), noticeably lower than those of the H_2 oxidation, which hence leads to the high selectivity to CO_2.

To summarize, we have shown that N-GR/Ni(111) is a highly active and selective catalyst for PROX. Key to this process is the activation of O_2 enabled by the Ni(111) support that covalently binds with the N-GR monolayer. As the nitrogen-doped graphene has been explored extensively in heterogeneous catalysis[41−44] and the encapsulation of metals by a graphene-like atomic monolayer was realized experimentally through a chemical vapor deposition process in mesoporous silica,[14] it can be expected that the N-GR/Ni(111) model catalyst proposed here can also be fabricated. Our prediction of N-GR/Ni(111) as oxidation catalyst is further supported by a recent experimental observation that cobalt nanoparticles encapsulated by nitrogen-doped carbon nanotubes are efficient catalysts for selective oxidation of hydrocarbons.[43] Apart from the favorable electronic interaction between N-GR and Ni, an advantage of the encapsulated structure is that N-GR can prevent Ni from being oxidized. Also, H_2 cannot easily diffuse through the N-GR layer and dissociate into adsorbed H atoms (the diffusion barrier is ~4 eV).

3.6. Ethylene Epoxidation on N-GR/Ni(111). Finally, we examined the possibility of N-GR/Ni(111) as a more general oxidation catalyst, and we investigated the ethylene epoxidation reaction over N-GR/Ni(111), which is commercialized over Ag/α-Al_2O_3 at 473−513 K using O_2 as the oxidant.[45,46] Because the annual production of ethylene oxide is over 20 million tons, increasing the selectivity to ethylene oxide and lowing the reaction temperature is highly desirable and an active area of research.[47] As an example, low-temperature (308 K) ethylene epoxidation was achieved over a mesoporous silicate using H_2O_2 as the oxidant.[46] Here, we present in Figure 10 the calculated energy profiles of ethylene epoxidation on N-GR/Ni(111). The physiosorbed ethylene on N-GR/Ni(111) reacts with oxygen through an Eley−Rideal mechanism after the facile dissociation of the chemisorbed O_2. Interestingly, because ethylene is not chemisorbed, an oxametallacycle intermediate[47] of ethylene epoxidation typical for silver catalysts that processes both ethylene oxide and acetaldehyde is avoided in the present case. Ethylene can react with the first oxygen readily with an effective energy barrier of 0.89 eV, while the second ethylene epoxidation has a higher barrier of 1.23 eV. The relatively difficult epoxidation of the second ethylene is due to the stronger adsorption energy of the second oxygen (see Table 1). Next, we developed and solved a steady-state microkinetic model for the epoxidation at 423 K with ethylene, oxygen, and ethylene oxide partial pressures of 10, 1, and 1 bar, respectively (see Table S9 for the model parameters). The TOF of ethylene oxide formation was calculated to be 0.41/s. The appreciable TOF suggests that N-GR/Ni(111) might also be a promising low-temperature ethylene epoxidation catalyst.

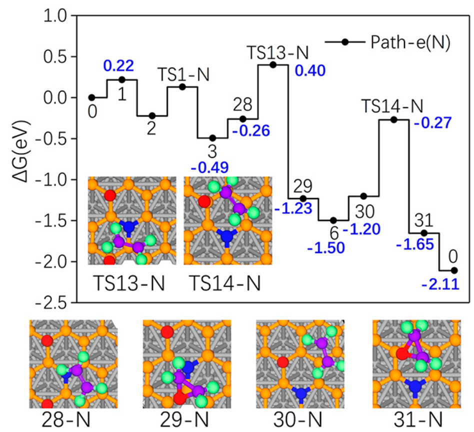

Figure 10. Free energy profiles of ethylene epoxidation on N-GR/Ni(111) at 423 K. The partial pressures of all gas-phase molecules are set to be 1 bar. The description of each elementary is also presented in Table S3.

Table 1. Adsorption Energy (Not Zero-Point Corrected in eV) of One Oxygen Atom (E_{ads}(O)) on Each Surface and One Hydrogen Atom on a Preadsorbed Oxygen (E_{ads}(H))[a]

	E_{ads}(O)	E_{ads}(H)
first oxygen of N-GR/Ni(111)	−0.44	−1.64
second oxygen of N-GR/Ni(111)	−0.87	−1.25
Ag(111)	−0.87	−1.53
Pd(111)	−1.72	−0.56
Pt(111)	−1.52	−0.38
Rh(111)	−2.41	−0.31

[a]The reference state is the clean surface and $0.5O_2$ and $0.5H_2$ molecules in the gas phase, respectively.

To understand the high activity of ethylene epoxidation on N-GR/Ni(111), we computed the adsorption energies of an oxygen atom and one hydrogen atom on a preadsorbed oxygen

https://dx.doi.org/10.1021/acscatal.0c00743
ACS Catal. 2020, 10, 5362−5370

on several surfaces. Table 1 shows that the adsorption behavior of O and H on N-GR/Ni(111) resembles that on Ag(111), while it contrasts those on Pd(111), Pt(111), and Rh(111). The similarity of oxygen and hydrogen adsorption on N-GR/Ni(111) and Ag(111) might be the origin for the high catalytic oxidation activity of N-GR/Ni(111).

4. CONCLUSIONS

We designed a N-GR/Ni(111) PROX catalyst through first-principles calculations. Ni(111)-supported boron-doped graphene was found to chemisorb O_2 with a significantly elongated O−O bond, leading to facile O−O dissociation. A carbon atom and its neighboring boron are the active sites for adsorption and reaction. While the CO oxidation on B-GR/Ni(111) is facile and the H_2 oxidation is much less active, we found that B-GR/Ni(111) is likely not a good PROX catalyst due to the energetically favorable formation of stable hydroxyl groups from the reaction of H_2O and adsorbed oxygen atoms on B-GR/Ni(111) that poison the catalyst. By contrast, N-GR/Ni(111) is highly active for CO oxidation in the presence of water. The two next-nearest carbon atoms of the nitrogen site are the active sites. Microkinetic modeling suggests that N-GR/Ni(111) is highly active and selective for PROX, with a TOF of O_2 consumption (300 K, CO pressure is 0.01 bar) and selectivity to CO_2 of 2.38/s and ∼100%, respectively. The effective free energy barrier of H_2 oxidation (at 1 bar H_2 pressure) is over 0.2 eV higher than that of CO (at 5×10^{-5} bar CO pressure) oxidation, ensuring the high selectivity to CO_2. N-GR/Ni(111) is also highly active for ethylene epoxidation at 423 K, and the TOF was calculated to be 0.41/s. The chemisorption of O_2 on B-GR/Ni(111) and N-GR/Ni(111) contrasts the physisorption of O_2 on free-standing B-GR and N-GR, which highlights the potential of the electronic atomic monolayer−metal support interaction for the design of novel oxidation catalysts.

■ ASSOCIATED CONTENT

Supporting Information

The Supporting Information is available free of charge at https://pubs.acs.org/doi/10.1021/acscatal.0c00743.

> Additional discussions on the choice of DFT functional, free energy profile of CO oxidation on hBN/Ni(111), relative energies for different B-GR adsorption configurations, transition state configurations of H_2 oxidation on B-GR/Ni(111), free energy profile of H_2 dissociation on B-GR/Ni(111), relative energies for different N-GR adsorption configurations, free energy profiles of CO and H_2 oxidation at various temperatures and pressures, and details of the microkinetic model (PDF)
>
> DFT structures of surface intermediates and transition states (PDF)

■ AUTHOR INFORMATION

Corresponding Author

Andreas Heyden − *Department of Chemical Engineering, University of South Carolina, Columbia, South Carolina 29208, United States;* orcid.org/0000-0002-4939-7489; Email: heyden@cec.sc.edu

Author

Yongjie Xi − *Department of Chemical Engineering, University of South Carolina, Columbia, South Carolina 29208, United States*

Complete contact information is available at: https://pubs.acs.org/10.1021/acscatal.0c00743

Notes

The authors declare no competing financial interest.

■ ACKNOWLEDGMENTS

We gratefully acknowledge financial support from the National Science Foundation (OIA-1632824). This research was performed using computing resources from EMSL (Ringgold ID 130367, Grant Proposal 49246), a DOE Office of Science User Facility sponsored by the Office of Biological and Environmental Research, and the National Energy Research Scientific Computing Center, a DOE Office of Science User Facility supported by the Office of Science of the U.S. Department of Energy under contract no. DE-AC02-05CH11231. This work was also supported by the South Carolina Smart State Center for Strategic Approaches to the Generation of Electricity (SAGE).

■ REFERENCES

(1) Landon, P.; Ferguson, J.; Solsona, B. E.; Garcia, T.; Al-Sayari, S.; Carley, A. F.; Herzing, A. A.; Kiely, C. J.; Makkee, M.; Moulijn, J. A.; Overweg, A.; Golunski, S. E.; Hutchings, G. J. Selective oxidation of CO in the presence of H2, H2O and CO2 utilising Au/α-Fe2O3 catalysts for use in fuel cells. *J. Mater. Chem.* **2006**, *16*, 199−208.

(2) Saavedra, J.; Whittaker, T.; Chen, Z.; Pursell, C. J.; Rioux, R. M.; Chandler, B. D. Controlling activity and selectivity using water in the Au-catalysed preferential oxidation of CO in H2. *Nat. Chem.* **2016**, *8*, 584.

(3) Cao, L.; Liu, W.; Luo, Q.; Yin, R.; Wang, B.; Weissenrieder, J.; Soldemo, M.; Yan, H.; Lin, Y.; Sun, Z.; Ma, C.; Zhang, W.; Chen, S.; Wang, H.; Guan, Q.; Yao, T.; Wei, S.; Yang, J.; Lu, J. Atomically dispersed iron hydroxide anchored on Pt for preferential oxidation of CO in H2. *Nature* **2019**, *565*, 631−635.

(4) Liu, K.; Wang, A.; Zhang, T. Recent Advances in Preferential Oxidation of CO Reaction over Platinum Group Metal Catalysts. *ACS Catal.* **2012**, *2*, 1165−1178.

(5) Qiao, B.; Wang, A.; Li, L.; Lin, Q.; Wei, H.; Liu, J.; Zhang, T. Ferric Oxide-Supported Pt Subnano Clusters for Preferential Oxidation of CO in H2-Rich Gas at Room Temperature. *ACS Catal.* **2014**, *4*, 2113−2117.

(6) Kuriyama, M.; Tanaka, H.; Ito, S.-i.; Kubota, T.; Miyao, T.; Naito, S.; Tomishige, K.; Kunimori, K. Promoting mechanism of potassium in preferential CO oxidation on Pt/Al2O3. *J. Catal.* **2007**, *252*, 39−48.

(7) Mariño, F.; Descorme, C.; Duprez, D. Noble metal catalysts for the preferential oxidation of carbon monoxide in the presence of hydrogen (PROX). *Appl. Catal., B* **2004**, *54*, 59−66.

(8) Kim, Y. H.; Park, E. D.; Lee, H. C.; Lee, D.; Lee, K. H. Preferential CO oxidation over supported noble metal catalysts. *Catal. Today* **2009**, *146*, 253−259.

(9) Galletti, C.; Specchia, S.; Saracco, G.; Specchia, V. Catalytic Performance of Rhodium-Based Catalysts for CO Preferential Oxidation in H2-Rich Gases. *Ind. Eng. Chem. Res.* **2008**, *47*, 5304−5312.

(10) Qiao, B.; Liu, J.; Wang, Y.-G.; Lin, Q.; Liu, X.; Wang, A.; Li, J.; Zhang, T.; Liu, J. Highly Efficient Catalysis of Preferential Oxidation of CO in H2-Rich Stream by Gold Single-Atom Catalysts. *ACS Catal.* **2015**, *5*, 6249−6254.

(11) Martínez-Arias, A.; Gamarra, D.; Hungría, A. B.; Fernández-García, M.; Munuera, G.; Hornés, A.; Bera, P.; Conesa, J. C.; Cámara,

A. L. Characterization of Active Sites/Entities and Redox/Catalytic Correlations in Copper-Ceria-Based Catalysts for Preferential Oxidation of CO in H2-Rich Streams. *Catalysts* **2013**, *3*, 378−400.
(12) Davó-Quiñonero, A.; Navlani-García, M.; Lozano-Castelló, D.; Bueno-López, A. CuO/cryptomelane catalyst for preferential oxidation of CO in the presence of H2: deactivation and regeneration. *Catal. Sci. Technol.* **2016**, *6*, 5684−5692.
(13) Rodriguez, J. A.; Liu, P.; Graciani, J.; Senanayake, S. D.; Grinter, D. C.; Stacchiola, D.; Hrbek, J.; Fernandez-Sanz, J. Inverse Oxide/Metal Catalysts in Fundamental Studies and Practical Applications: A Perspective of Recent Developments. *J. Phys. Chem. Lett.* **2016**, *7*, 2627−39.
(14) Cui, X.; Ren, P.; Deng, D.; Deng, J.; Bao, X. Single layer graphene encapsulating non-precious metals as high-performance electrocatalysts for water oxidation. *Energy Environ. Sci.* **2016**, *9*, 123−129.
(15) Xi, Y.; Heyden, A. Direct Oxidation of Methane to Methanol Enabled by Electronic Atomic Monolayer−Metal Support Interaction. *ACS Catal.* **2019**, *9*, 6073−6079.
(16) Dahal, A.; Batzill, M. Graphene−nickel interfaces: a review. *Nanoscale* **2014**, *6*, 2548−2562.
(17) Auwärter, W. Hexagonal boron nitride monolayers on metal supports: Versatile templates for atoms, molecules and nanostructures. *Surf. Sci. Rep.* **2019**, *74*, 1−95.
(18) Agnoli, S.; Favaro, M. Doping graphene with boron: a review of synthesis methods, physicochemical characterization, and emerging applications. *J. Mater. Chem. A* **2016**, *4*, 5002−5025.
(19) Usachov, D.; Vilkov, O.; Grüneis, A.; Haberer, D.; Fedorov, A.; Adamchuk, V. K.; Preobrajenski, A. B.; Dudin, P.; Barinov, A.; Oehzelt, M.; Laubschat, C.; Vyalikh, D. V. Nitrogen-Doped Graphene: Efficient Growth, Structure, and Electronic Properties. *Nano Lett.* **2011**, *11*, 5401−5407.
(20) Kresse, G.; Furthmuller, J. Efficient iterative schemes for ab initio total-energy calculations using a plane-wave basis set. *Phys. Rev. B: Condens. Matter Mater. Phys.* **1996**, *54*, 11169.
(21) Kresse, G.; Furthmuller, J. Efficiency of ab-initio total energy calculations for metals and semiconductors using a plane-wave basis set. *Comput. Mater. Sci.* **1996**, *6*, 15−50.
(22) Perdew, J. P.; Burke, K.; Ernzerhof, M. Generalized gradient approximation made simple. *Phys. Rev. Lett.* **1996**, *77*, 3865.
(23) Blöchl, P. E. Projector augmented-wave method. *Phys. Rev. B: Condens. Matter Mater. Phys.* **1994**, *50*, 17953−17979.
(24) Kresse, G.; Joubert, D. From ultrasoft pseudopotentials to the projector augmented-wave method. *Phys. Rev. B: Condens. Matter Mater. Phys.* **1999**, *59*, 1758−1775.
(25) Monkhorst, H. J.; Pack, J. D. Special Points for Brillouin-Zone Integrations. *Phys. Rev. B* **1976**, *13*, 5188.
(26) Grimme, S.; Antony, J.; Ehrlich, S.; Krieg, H. A consistent and accurate ab initio parametrization of density functional dispersion correction (DFT-D) for the 94 elements H-Pu. *J. Chem. Phys.* **2010**, *132*, 154104.
(27) Hammer, B.; Hansen, L. B.; Nørskov, J. K. Improved adsorption energetics within density-functional theory using revised Perdew-Burke-Ernzerhof functionals. *Phys. Rev. B: Condens. Matter Mater. Phys.* **1999**, *59*, 7413−7421.
(28) Zhang, Y.; Yang, W. Comment on ″Generalized Gradient Approximation Made Simple″. *Phys. Rev. Lett.* **1998**, *80*, 890−890.
(29) Peng, H.; Yang, Z.-H.; Perdew, J. P.; Sun, J., Versatile van der Waals Density Functional Based on a Meta-Generalized Gradient Approximation. *Phys. Rev. X* **2016**, *6*. DOI: 10.1103/PhysRevX.6.041005
(30) Henkelman, G.; Uberuaga, B. P.; Jonsson, H. A climbing image nudged elastic band method for finding saddle points and minimum energy paths. *J. Chem. Phys.* **2000**, *113*, 9901−9904.
(31) Henkelman, G.; Jónsson, H. A dimer method for finding saddle points on high dimensional potential surfaces using only first derivatives. *J. Chem. Phys.* **1999**, *111*, 7010−7022.
(32) Heyden, A.; Bell, A. T.; Keil, F. J. Efficient methods for finding transition states in chemical reactions: comparison of improved dimer method and partitioned rational function optimization method. *J. Chem. Phys.* **2005**, *123*, 224101.
(33) Xu, H.; Cheng, D.; Cao, D.; Zeng, X. C. A universal principle for a rational design of single-atom electrocatalysts. *Nature Catalysis* **2018**, *1*, 339−348.
(34) Gómez Díaz, J.; Ding, Y.; Koitz, R.; Seitsonen, A. P.; Iannuzzi, M.; Hutter, J. Hexagonal boron nitride on transition metal surfaces. *Theor. Chem. Acc.* **2013**, *132*, 1350.
(35) Henkelman, G.; Arnaldsson, A.; Jonsson, H. A fast and robust algorithm for Bader decomposition of charge density. *Comput. Mater. Sci.* **2006**, *36*, 354−360.
(36) Kozuch, S. Steady State Kinetics of Any Catalytic Network: Graph Theory, the Energy Span Model, the Analogy between Catalysis and Electrical Circuits, and the Meaning of "Mechanism. *ACS Catal.* **2015**, *5*, 5242−5255.
(37) Zhao, S.; Chen, F.; Duan, S.; Shao, B.; Li, T.; Tang, H.; Lin, Q.; Zhang, J.; Li, L.; Huang, J.; Bion, N.; Liu, W.; Sun, H.; Wang, A.-Q.; Haruta, M.; Qiao, B.; Li, J.; Liu, J.; Zhang, T. Remarkable active-site dependent H2O promoting effect in CO oxidation. *Nat. Commun.* **2019**, *10*, 3824.
(38) González-Herrero, H.; Gómez-Rodríguez, J. M.; Mallet, P.; Moaied, M.; Palacios, J. J.; Salgado, C.; Ugeda, M. M.; Veuillen, J.-Y.; Yndurain, F.; Brihuega, I. Atomic-scale control of graphene magnetism by using hydrogen atoms. *Science* **2016**, *352*, 437−441.
(39) Hollen, S. M.; Gupta, J. A. Painting magnetism on a canvas of graphene. *Science* **2016**, *352*, 415−416.
(40) Saavedra, J.; Doan, H. A.; Pursell, C. J.; Grabow, L. C.; Chandler, B. D. The critical role of water at the gold-titania interface in catalytic CO oxidation. *Science* **2014**, *345*, 1599−1602.
(41) Wang, H.; Maiyalagan, T.; Wang, X. Review on Recent Progress in Nitrogen-Doped Graphene: Synthesis, Characterization, and Its Potential Applications. *ACS Catal.* **2012**, *2*, 781−794.
(42) Zhou, W.; Zhou, J.; Zhou, Y.; Lu, J.; Zhou, K.; Yang, L.; Tang, Z.; Li, L.; Chen, S. N-Doped Carbon-Wrapped Cobalt Nanoparticles on N-Doped Graphene Nanosheets for High-Efficiency Hydrogen Production. *Chem. Mater.* **2015**, *27*, 2026−2032.
(43) Lin, X.; Nie, Z.; Zhang, L.; Mei, S.; Chen, Y.; Zhang, B.; Zhu, R.; Liu, Z. Nitrogen-doped carbon nanotubes encapsulate cobalt nanoparticles as efficient catalysts for aerobic and solvent-free selective oxidation of hydrocarbons. *Green Chem.* **2017**, *19*, 2164−2173.
(44) Su, H.; Zhang, K.-X.; Zhang, B.; Wang, H.-H.; Yu, Q.-Y.; Li, X.-H.; Antonietti, M.; Chen, J.-S. Activating Cobalt Nanoparticles via the Mott−Schottky Effect in Nitrogen-Rich Carbon Shells for Base-Free Aerobic Oxidation of Alcohols to Esters. *J. Am. Chem. Soc.* **2017**, *139*, 811−818.
(45) Özbek, M. O.; van Santen, R. A. The Mechanism of Ethylene Epoxidation Catalysis. *Catal. Lett.* **2013**, *143*, 131−141.
(46) Yan, W.; Ramanathan, A.; Ghanta, M.; Subramaniam, B. Towards highly selective ethylene epoxidation catalysts using hydrogen peroxide and tungsten- or niobium-incorporated mesoporous silicate (KIT-6). *Catal. Sci. Technol.* **2014**, *4*, 4433−4439.
(47) Pu, T.; Tian, H.; Ford, M. E.; Rangarajan, S.; Wachs, I. E. Overview of Selective Oxidation of Ethylene to Ethylene Oxide by Ag Catalysts. *ACS Catal.* **2019**, *9*, 10727−10750.